Science Advances
AAAS

advances.sciencemag.org/cgi/content/full/7/2/eabe4080/DC1

Supplementary Materials for

Isomer-specific kinetics of the $C^+ + H_2O$ reaction at the temperature of interstellar clouds

Tiangang Yang, Anyang Li, Gary K. Chen, Qian Yao, Arthur G. Suits, Hua Guo*, Eric R. Hudson*, Wesley C. Campbell*

*Corresponding author. Email: wes@physics.ucla.edu (W.C.C.); eric.hudson@ucla.edu (E.R.H.); hguo@unm.edu (H.G.)

Published 6 January 2021, *Sci. Adv.* **7**, eabe4080 (2021)
DOI: 10.1126/sciadv.abe4080

This PDF file includes:

Supporting Information

1. Characterization of Cryogenic Buffer Gas Beam (CBGB)

Gaining a quantitative understanding of the reaction temperature in the beam + trap scenario in this work requires characterization of the velocity of the target species entrained within the buffer gas beam. For this, we employ an atomic tracer species that can be directly detected in small amounts. Ytterbium metal is known to have good ablation properties and the produced neutral isotopes have well known isotope shifts and hyperfine splittings. By ablating ytterbium foil inside of the cryogenic cell while the neon gas is being introduced, the ytterbium is cooled by the buffer gas and carried out of the cell. As long as the target species number density is a trace amount in comparison to the bulk buffer gas number density (0.1%), the flow characteristics are dominated by the buffer gas species(*50*). To determine the velocity of the beam, we use a 399 nm laser to excite the Yb and fluorescence is detected. The laser is scanned over 3 GHz, encompassing all naturally occurring Yb isotope transitions. Two scans are taken, one with the 399 nm light perpendicular to the beam path (transverse), and the other with the laser at an angle of $\theta = 57.3°$ relative to the beam, shown in Figure S1. Since the individual transitions are all thermally broadened well beyond the natural linewidth, the spectrum is fitted with summed Gaussian functions with predetermined isotopic shifts taken from literature. This yields the center frequency as well as the thermally broadened width of the lines. Between the transverse and angled scans, we find an offset in the spectrum caused by the doppler shift, seen in figure S2,

$$\Delta f = \frac{\Delta v}{v} f \cos(\theta), \qquad \text{(S1)}$$

where f is the rest-frame center frequency, Δf is the offset observed, v is the forward

velocity of the excited Yb, and θ is the angle of the atomic beam with respect to the excitation laser beam. The fitted shared widths indicate a beam temperature of (20 ± 1) K, which is the temperature of the cryogenic cell. Using equation S1, the forward velocity of the beam is $\approx \frac{(150 \pm 3)\mathrm{m}}{\mathrm{s}}$, in good agreement with a mildly boosted neon buffer gas of equilibrium temperature 20 K. The neon buffer gas densities are sufficient to ensure that the water seeded into the beam makes 100s of collisions before extraction into a ballistic beam. These 100s of collisions ensure that the internal rotational states of the water have reached 20 K. Before extraction, the translational degrees of freedom have also reached 20 K, however, extraction of a beam operating within the intermediate flow regime causes collisions at the aperture, providing slight forward boosting of its forward velocity as well as narrowing of the velocity distribution. In the center-of-mass frame, the reaction occurs with an internal temperature for the H_2O of ~10-15 K (given by $\frac{E}{kb} = \frac{\mu v_{rel}^2}{2kb}$, μ is reduced mass). We report this collision energy as ~20 K in the manuscript to convey that it is an approximate collision energy. Due to the anisotropic boosting, the velocity doesn't follow a Maxwell Boltzmann distribution, and we cannot make many concrete statements about it, except that it is narrower than a Maxwell Boltzmann.

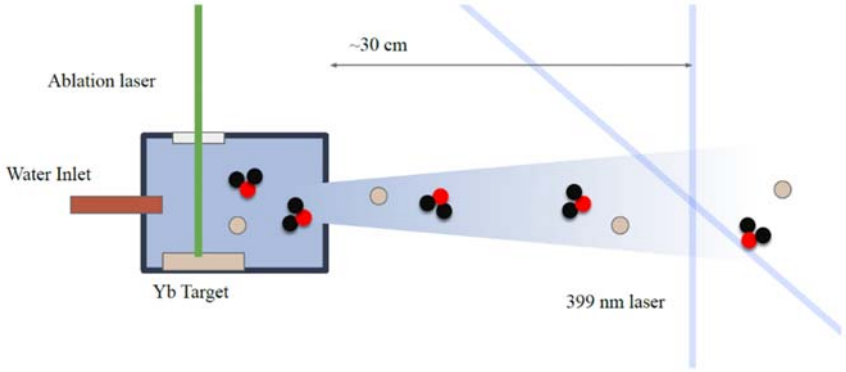

Figure S1. Diagram of entrained neutral Yb calibration of the CBGB. H_2O and Yb are co-entrained in a buffer gas

of neon. The 399 nm laser is scanned over 3 GHz, recording the Yb LIF spectrum both transverse, and at a $57.3°$ angle, to the beam.

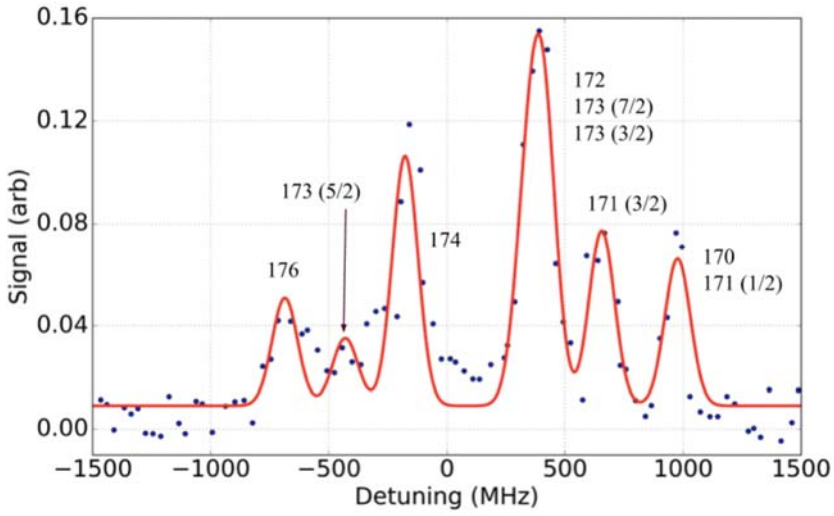

Figure S2. Angled longitudinal scan of Yb fluorescence collected by a PMT ≈ 24 cm from the cell aperture. The frequency indication is relative to the measured ^{174}Yb frequency from the scan with the excitation laser perpendicular to the atomic beam. A fit of Gaussians on the observed Yb isotopic transitions is shown with fixed relative line centers, while a shared width and the individual heights are fitting parameters. Fits yield a forward velocity of $\approx (150 \pm 3)$ m/s and broadened width of (20 ± 1) K. We find that the Yb is entrained within the neon and sympathetically cooled to the cryogenic cell's temperature. The water that is also introduced in the beam will be at a similar temperature and forward velocity since the beam dynamics is dominated by the properties of the buffer gas species – that is, since the neon density is much larger than that of the water(*51*).

To control the beam flux, we insert a vacuum compatible Optical Shutter (Uniblitz VS35) in the molecular beam line. The shutter does not create a seal within the chamber, and background gas molecules can potentially find their way around and influence the beam.

To measure the H_2O in the beam directly and ascertain the effectiveness of the shutters, we use two methods. First, we use a residual gas analyzer (RGA) in the beam path. By opening and closing shutters in the beam path we observe a clear, prompt extinction of the water signal. Second, we use the ions in the trap themselves to observe the beam and constrain any background water. Trapped Be^+ ions react with H_2O to predominately produce $BeOH^+$, which we see as a drop in the fluorescence in Figure S3 and Figure S4. These figures compare the fluorescence decay as a beam from the CBGB is blocked by in vacuo shutter in the beam line to the unblocked case. Examining the fitted reaction rates, we find that they agree with the background reaction rate shown in figure S4. This indicates that a beam of cryogenic water is impinging upon the trapped ions and reactions of background H_2O are insignificant relative to the other reaction rates.

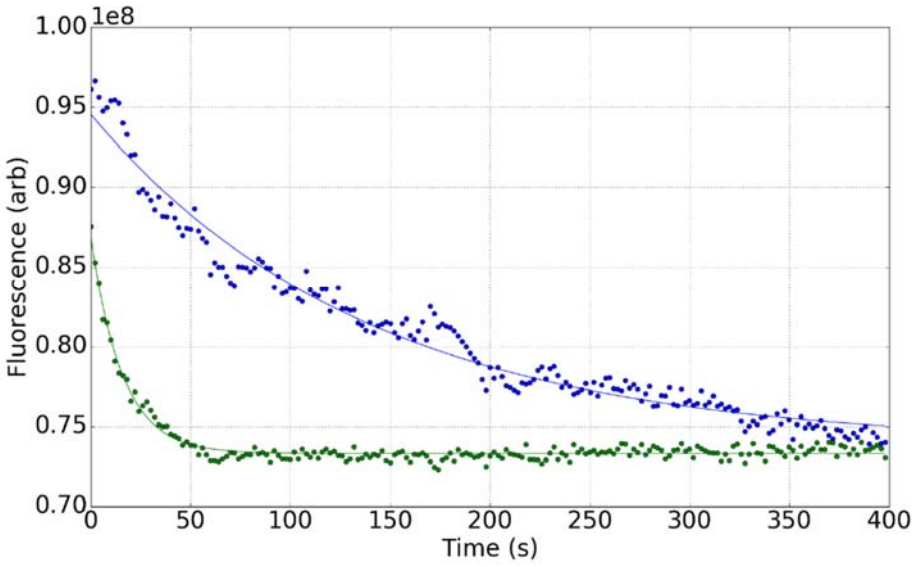

Figure S3. Fluorescence decay of trapped Be^+ ions exposed to a cryogenic water beam with an inline shutter in vacuo either opened, in green ($\tau = 7.2 \times 10^{-3}$ s) or closed, in blue ($\tau = 63.7 \times 10^{-3}$ s)

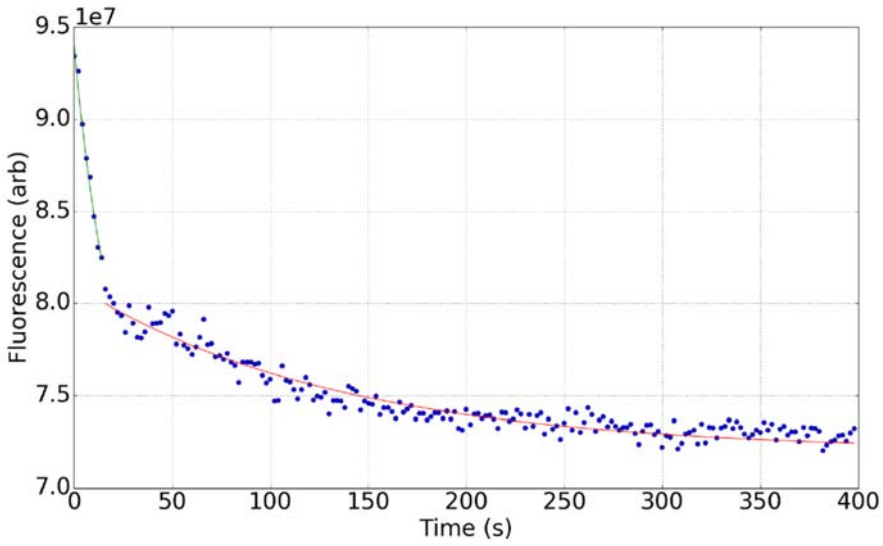

Figure S4. Fluorescence decay of trapped Be^+ ions exposed to a cold-water beam with the inline shutter closed at $t \approx 25$ s. Fits to the decay with the shutter open vs. closed yield Be^+ lifetime of $\tau = 7.6 \times 10^{-3}$ s and $\tau = 53.7 \times 10^{-3}$ s, respectively.

2. Proton transfer reactions

To distinguish the two isomers of the formyl ion produced in the title reaction, we use proton transfer reactions with $^{15}N_2$. This choice is based on a number of factors explained in this section.

A general form of the desired titration reaction for analyzing the isomeric branching ratio with species X is:

$HOC^+ + X \rightarrow XH^+ + CO$

$HCO^+ + X \rightarrow$ No Reaction

In selecting a titration gas, the most important property, other than possessing a proton affinity

between the two isomers, is a low reactivity with the other trapped species. If the titration gas reacts with Be^+, C^+, or any other ionized species in the trap, it can be difficult to disambiguate the products and the branching ratio measurement may be affected. Table 1, shows candidate titration gases with proton affinity between 4.43 eV and 6.16 eV that only react with HOC^+. The previous measurement of the branching ratio used in a selected ion flow tube (SIFT) instrument used N_2O at 305 K. Further, rate coefficients for reactions with O_2, Kr, Xe, CO, CO_2, and CH_4 have been explored (*22, 52*). In our work, we explored titration with Xe, CO_2, CH_4, N_2O, and $^{15}N_2$.

The reaction of N_2O and Be^+ has not been previously studied. We observed multiple subsequent reactions occurring that lead to loss of Be^+ without replacement by another ion – i.e. overall trap loss. This is typically only possible when a much heavier charged product is produced that is not stable in the ion trap. Without the coolant ion, the mass resolution of the TOF declines significantly making discrimination of the target masses difficult. Further, N_2O is known to react with C^+ to make NO^+ and CN with a total rate coefficient of 9.1×10^{-10} cm^3/s at 300 K (*53*), which adds more complexity to the mass spectra. Similarly, CH_4 reacted with the trapped C^+, producing new *m/z* peaks in the mass spectra due to both direct and higher-order reactions. With Xe, the charged product XeH^+ has a mass to charge ratio of *m/z* = 132, which was not stable in our trap.

For these reasons, we chose not to use N_2O, CH_4, or Xe as titration gases and instead used N_2. N_2 has several benefits including ease of use and a lack of strong reaction with C^+ or Be^+. N_2 had not previously been used in the literature, most likely because the reaction product N_2H^+ has nearly the same *m/z* as the formyl ion isomer, making mass spectrometry difficult to apply.

We circumvented this problem by using the rarer isotope, $^{15}N_2$.

Table S1: Proton affinities of gasses between formyl isomers where (*) indicates H bonding location (*54*).

	Affinity (kJ/mol)	Affinities (eV)
O_2	422	4.37
H_2	424	4.39
Kr	425	4.40
CO*	427	4.43
HF	490	5.08
N_2	495	5.13
Xe	496	5.14
NO	531	5.50
CO_2	548	5.68
CH_4	552	5.72
HCl	564	5.85
HBr	569	5.90
N_2O	571	5.92
*CO	594	6.16

3. Experimental Sequence and Chemical Rate Equations

3.1 Experimental sequence

A typical experimental sequence and ion "cloud" image are shown in Fig. S5. C^+ ions are first loaded and sympathetically cooled by Be^+ ions in the ion trap. Typically, hundreds of ions are trapped, but not crystallized into a Coulomb crystal, shown on the bottom of Fig. S5. In the un-crystallized phase, dark C^+ ions sit at the trap center and are surrounded by laser cooled, fluorescing, Be^+ ions. The 20 K, H_2O beam is then introduced into the trap for 20 s and reactions occur. The beam is then blocked by the in vacuo molecular beam shutter (100 ms response time) and (on a 1 second timescale) a gate valve. An approximately one second delay is provided to allow the internally excited product ions to isomerize and/or relax to their

vibrational ground state via radiative decay (*43*). Next, the $^{15}N_2$ titrant gas is introduced via a room-temperature leak valve for approximately 10 s. Afterwards, all ions are ejected into the TOF-MS.

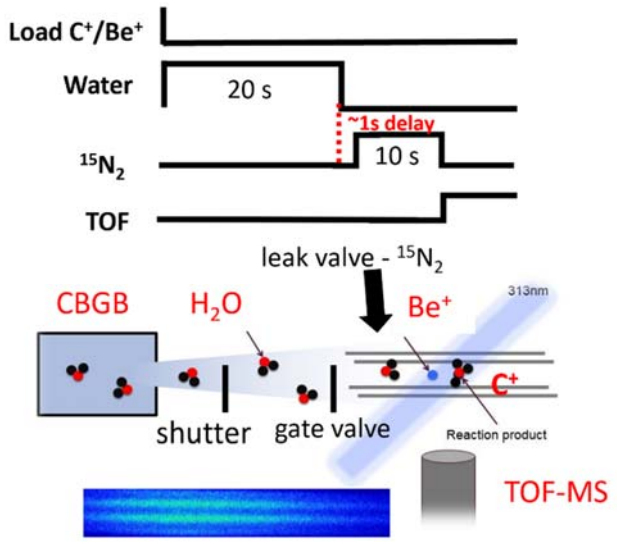

Figure S5. A schematic diagram of the experimental setup, time sequence and ion cloud.

3.2 The production of the formyl isomers and subsequent reactions with water: mathematical model

In this section, we consider in experimental detail the following reactions in the main text:

$$C^+ + H_2O \rightarrow HOC^+ + H \qquad (1)$$

$$C^+ + H_2O \rightarrow HCO^+ + H \qquad (2)$$

$$[HCO]^+ + H_2O \rightarrow H_3O^+ + CO. \qquad (5\text{-}6)$$

We treat the case in which the water density in the beam is constant, and assume that pseudo first order kinetics applies. The differential forms of the densities subject to the above reactions are

$$\dot{C}(t) = -k_{1+2}\rho_{H_2O}C(t)$$

$$[H\dot{C}O](t) = \rho_{H_2O}(k_{1+2}C(T) + k_5[HCO](T))$$

$$H_3\dot{O}(t) = k_5\rho_{H_2O}[HCO](T)$$

where $C(t)$ is the carbon ion density, $[HCO](t)$ is the density of both isomers of the formyl ion, ρ_{H_2O} is the density of water, and $H_3O(t)$ is the density of H_3O^+. These differential equations are solved by,

$$C(t) = C_0 e^{-k_{1+2}\,\rho_{H_2O}t} \quad \text{(S2)}$$

$$HCO(t) = \frac{e^{-(k_{1+2}+k_5)\rho_{H_2O}t}}{k_{1+2}-k_5}\left(e^{k_{1+2}\rho_{H_2O}t}((C_0 + [HCO]_0)k_{1+2} - [HCO]_0 k_5 - C_0 e^{-(k_{1+2}+k_5)\rho_{H_2O}t}\right) \quad \text{(S3)}$$

$$H_3O(t) = H_3O_0 + [HCO]_0\left(1 - e^{-k_5\rho_{H_2O}t}\right) + \frac{C_0(k_{1+2}\left(1-e^{-k_5\rho_{H_2O}t}\right)+k_5\left(e^{-k_{1+2}\rho_{H_2O}t}-1\right))}{k_{1+2}-k_5}. \quad \text{(S4)}$$

3.3 The reactions of the isomers $[HCO]^+$ with titration gas $^{15}N_2$

For the reactions

$HOC^+ + {}^{15}N_2 \rightarrow {}^{15}N_2H^+ + CO$ (3)

and

$HCO^+ + {}^{15}N_2 \rightarrow$ No reaction, (4)

the differential form of the densities of these species is given by

$$H\dot{O}C^+(t) = -k_3\rho HOC^+(t)$$

and

$^{15}N_2\dot{H}^+(t) = k_3\rho HOC^+(t)$,

with $HOC^+(t)$ the density of HOC+, ρ the density of $^{15}N_2$, and $^{15}N_2H^+(t)$ the density of $^{15}N_2H^+$.

Since we do not distinguish between HOC^+ and HCO^+ in the mass spectra, the mass spectrum reveals only the value of

$[HCO]^+(t) = HOC^+(t) + HCO^+(t)$.

Due to the unreactivity of HCO^+ with N_2 (reaction 4), $HCO(t) = HCO_0$, the initial density of HCO^+ formed by the title reaction. The solutions to the observable densities, then, are

$$[HCO]^+(t) = HOC_0^+ e^{-k_3\rho t} + HCO_0^+ \quad \text{(S5)}$$

$$^{15}N_2H^+(t) = HOC_0^+(1 - e^{-k_3\rho t}) + {}^{15}N_2H_0^+ \quad \text{(S6)}$$

Manipulation of solutions S5 and S6, setting $^{15}N_2H_0^+ = 0$, yields the ratio of N_2H^+ and $[HCO]^+$,

$$\frac{^{15}N_2H^+(t)}{^{15}N_2H^+(t)+[HCO]^+(t)} = \zeta(1 - e^{k_3\rho t}) \quad \text{(S7)}$$

where $\zeta \equiv \frac{HOC_0}{HOC_0+HCO_0}$. As shown in Fig. 1(C) and described above, to distinguish the isomers $[HCO]^+$, the $^{15}N_2$ titrant gas is introduced via a room-temperature leak valve for approximately 10 s. Repeating this process over various densities of $^{15}N_2$ allows us to determine the isomer branching ratio as well as the proton transfer rate constant. A fit performed on the data over various densities (refer to Fig.1(C) in the main text) yields a rate constant of $k_3 = (6.6 \pm 1.0) \times 10^{-10}$ cm^3/s, and a final branching ratio of HOC^+ to HCO^+ is 1.4 (2). The

error bars here are the statistical errors. and we estimate another 30% systematic errors for the rate constants due to the measurement of absolute density. The details about the density measurement can be found in our previous work(*34*). The branching ratio is independent of the absolute H_2O density, because these are measured in the same H_2O gas.

3.4 Verification of N_2 proton affinity

As described in the main text, (5) and (6) are the secondary reactions in our system. Though the appearance of H_3O^+ presents no problem for our study, a *relative* rate difference between these two reactions ((5) and (6)) at low temperature would systematically shift the trapped HOC^+/HCO^+ ratio and cause an error in the determination of branching ratio η. To constrain this potential error, we repeat the sequence described above in the presence of a large amount of neutral CO gas to produce samples with varying compositions of HCO^+ and HOC^+ via reaction (7).

$$HCO^+ + H_2O \rightarrow H_3O^+ + CO, \quad (5)$$

$$HOC^+ + H_2O \rightarrow H_3O^+ + CO. \quad (6)$$

$$HOC^+ + CO \rightarrow HCO^+ + CO. \quad (7)$$

CO is introduced continuously via the leak valve in the differential cross region to produce a pressure of $\approx 4 \times 10^{-9}$ Torr as measured in the trap chamber. The constant introduction of CO ensures full conversion of HOC^+ to HCO^+ at a rate ~10 times faster than that of reactions (1) and (2) ensuring we observe the time evolution of reaction (5) as seen in Figure S6b. A

similar procedure of continuously exposing the trap to the CBGB without CO yields a combination of the rates of reactions (5) and (6), also shows as reaction (5-6) is seen in Figure S6a).

The rates of reactions (1), (5), and reaction (5-6) are found with least-squares fitting of the solutions to differential equations found above. Beam densities are determined for each run individually by considering the $Be^+ + H_2O$ reaction.

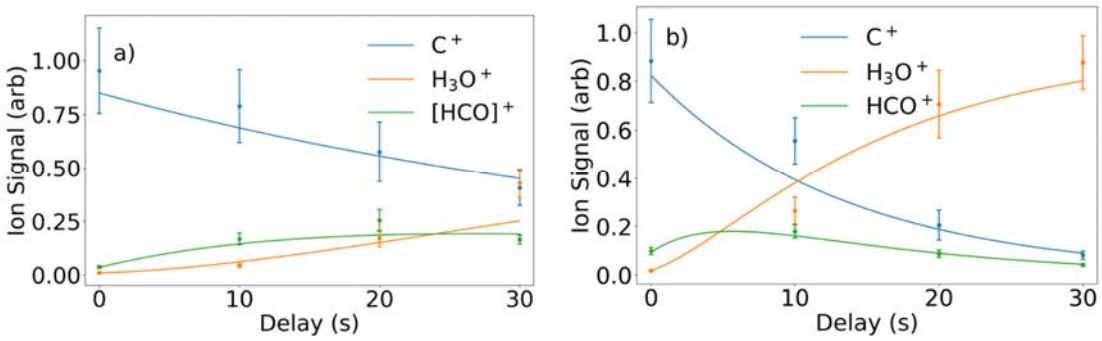

Figure S6. Time evolution of C^+ and H_2O introduced via CBGB as well as subsequent reaction products. a) TOF traces without flooding of CO where fitted rate constants are found to be $k_1 + k_2 = (7.7 \pm 0.6) \times 10^{-9}$ cm^3/s, and $k_5 = (1.7 \pm 0.2) \times 10^{-8}$ cm^3/s. b) TOF traces with flooding of CO where fitted rate constants are found to be $k_1 + k_2 = (7.9 \pm 0.6) \times 10^{-9}$ cm^3/s, and $k_5 = (1.7 \pm 0.2) \times 10^{-8}$ cm^3/s.

By producing only HCO^+, we directly observe the reaction (5) at cold temperature and measure the rate coefficient to be $k_5 = (1.7 \pm 0.2) \times 10^{-8}$ cm^3/s. Although we cannot directly measure the rate coefficient of reaction (6), we repeat this measurement with or without the presence of CO and, therefore, to make the pure HCO^+ or the combination of HCO^+ and HOC^+ We find there is no deviation between the pure $HCO^+ + H_2O$ and $[HCO]^+ + H_2O$ (recall that $[HCO]^+$ represents the combination of the two isomers). Thus, we use the measured k_5 for both reactions (5) and (6). Theoretically, the similar rate constant may not be surprising

given that the only difference at the capture theory level between reactions (5) and (6) comes from the short-ranged, dipole-dipole portion of the interaction, which is much weaker than the ion-dipole and ion-quadrupole contributions.

Typical TOF-MS data for this procedure is shown in Fig. 1(D), and show no production of any $^{15}N_2H^+$. Therefore, we conclude that both a pure HCO^+ sample can be prepared with the presence of CO in the ion trap (*52*) and reaction (4) is indeed energetically forbidden.

3.5 Isomerization by H_2O

Additionally, in principle, H_2O could isomerize the isoformyl ion in a second order reaction according to $HOC^+ + H_2O \rightarrow HCO^+ + H_2O$. However, H_2O readily captures a proton from HOC^+, and because its proton affinity is greater than both HCO^+ and HOC^+ (see table S1), it does not return the proton to the carbon end of CO to give HCO^+. Instead, it is energetically profitable for the water to retain the proton and form $CO + H_3O^+$ rather, *i.e.*, reactions (6), and isomerization by H_2O does not occur (*45*).

4. Quasi-classical trajectory calculations on $N_2 + HOC^+ \rightarrow N_2H^+ + CO$ and $N_2 + HCO^+$

The product branching of this process is of great importance to determine the product branching ratio of the $C^+ + H_2O$ reaction because of the titration scheme used in the experiment. To this end, some of the authors have recently published a global potential energy surface (PES) and performed dynamical calculations using quasi-classical trajectory (QCT) (*47*). Here, we have improved the original PES by adding long-range terms needed to understand low-temperature dynamics. Specifically, the following long-range interaction between N_2 and HOC^+ is used:

$$V_{int}(R,\theta) = V_{q\Theta}(R,\theta) + V_{q\alpha}(R,\theta) = \frac{q\Theta(3cos^2\theta-1)}{2R^3} - \frac{q^2[\alpha+\frac{\alpha_\parallel-\alpha_\perp}{3}(3cos^2\theta-1)]}{2R^4}, \quad \text{(S8)}$$

where R denotes the distance between the center of mass of N_2 and O and θ the angle between the R vector and the N-N bond. Here the HOC^+ is approximated as a point charge located on O. The quadrupole of N_2 is -1.47 Debye·Å, and its polarizabilities are given as $\alpha = 1.767$ Å^3, $\alpha_\parallel - \alpha_\perp = 0.69$ Å^3. This long-range potential consists of the interaction potential and the potentials for the molecules

$$V_{LR} = V_{int} + V_{N_2} + V_{HOC^+}, \quad \text{(S9)}$$

which is connected with the short-range one (*47*)

$$V_{PES} = SV_{SR} + (1-S)V_{LR}, \quad \text{(S10)}$$

using the switching function:

$$S = \frac{1-\tanh[2(R-6.5\text{Å})]}{2}. \quad \text{(S11)}$$

With this long-range corrected PES, we have recalculated the branching between the N_2H^+ + CO and N_2 + HCO^+ channels at experimental conditions using 5000 trajectories, and found that the isomerization channel (N_2 + HCO^+) has a 18% probability. The details of the calculation can be found in Ref. (*47*).

5. Quasi-classical trajectory calculations on the C^+ + H_2O reaction

The global PES for the $C^+(^2P)$ + $H_2O(X^1A_1)$ → $HCO^+/HOC^+(X^1\Sigma^+)$ + $H(^2S)$ reaction consists of a long-range (LR) term in the reactant asymptote and a short-range (SR) term for the strongly interaction region. The former, which is important for an accurate description of the reaction kinetics, accounts for the leading electrostatic interactions between the two reactants when they are far apart. The latter, on the other hand, is obtained by fitting ab initio data. The two segments of the PES are connected smoothly via a switching function, S_{global}:

$$V = S_{global}V_{\mathrm{SR}} + \left(1 - S_{global}\right)V_{\mathrm{LR}}, \quad \text{(S12)}$$

$$S_{global} = \frac{1-\tanh[3(\xi-9.0)]}{2}, \quad \text{(S13)}$$

where ξ is the distance (in Å) between C and O. the PES is dominated by V_{LR} for ξ > 9.5 Å, while by V_{SR} for ξ < 8.5 Å.

The LR PES can be written as:

$$V_{\mathrm{LR}} = V_{\mathrm{H_2O}} + V_{\mathrm{ES}}, \quad \text{(S14)}$$

where $V_{\mathrm{H_2O}}$ is the PES for the isolated H_2O molecule. This local PES is developed by a three-dimensional cubic spline interpolation of 1274 *ab initio* points at the explicitly correlated unrestricted coupled cluster singles, doubles, and perturbative triples (UCCSD(T)) method (*55*) with a specially optimized triples zeta correlation consistent F12 basis set (VTZ-F12) level (*56*), the same as the SR PES calculations (*vide infra*). All the potential energies of *ab initio* points are related to the potential minimum of H_2O at its equilibrium geometry. The electrostatic interactions V_{ES} between the C^+ ion and H_2O molecule consist of several long-range terms. In describing these interactions, we assume that the water molecule is in its equilibrium geometry with the O atom in the *z* axis and the molecule is in the *yz* plane. *R* is the distance between C^+ ion and the center of mass of H_2O. We define θ_x, θ_y and θ_z as the angles between the $\vec{R}$ vector and *x, y* and *z* axes, respectively. The leading electrostatic terms include the charge-dipole (proportional to R^{-2}), charge-quadruple (proportional to R^{-3}), and charge-induced dipole (proportional to R^{-4}) interactions (*57, 58*):

$$V_{\mathrm{ES}} = V_{\mathrm{c-d}} + V_{\mathrm{c-q}} + V_{\mathrm{c-id}}, \quad \text{(S15)}$$

where the charge-dipole interaction potential is:

$$V_{\mathrm{c-d}} = q\mu_{\mathrm{H_2O}}R^{-2}\cos\theta_z, \quad \text{(S16)}$$

the charge-quadruple interaction potential is:

$$V_{\mathrm{c-q}} = \frac{1}{2} qR^{-3}\left[\Theta_{zz}(3\cos^2\theta_z - 1) + \Theta_{xx}(3\cos^2\theta_x - 1) + \Theta_{yy}\left(3\cos^2\theta_y - 1\right)\right] \quad \text{(S17)}$$

and the charge-induced dipole interaction potential is:

$$V_{\mathrm{c-id}} = -\frac{1}{2} q\alpha R^{-4}\left[1 + \frac{\left|\alpha_{zz} - 1/2(\alpha_{xx} + \alpha_{yy})\right|}{3\alpha}(3\cos^2\theta_z - 1)\right]. \quad \text{(S18)}$$

For the H_2O molecule, the dipole moment μ_{H_2O} is 1.855 Debye, the three non-zero quadruple moments Θ_{xx}, Θ_{yy} and Θ_{zz} are -2.5, 2.63 and -0.13 Debye Å, and the polarizability α is 9.92 a.u. (α_{xx}, α_{yy} and α_{zz} are 10.31, 9.55 and 9.91 a.u.).

For the SR PES, we first carried out *ab initio* calculations using the UCCSD(T)-F12a method with a basis set VTZ-F12. The stationary points along the reaction path are shown in Figure 2 and their geometries and energies are listed in Table S2. These *ab initio* points are then fitted using the high-fidelity permutation invariant polynomial-neural network (PIP-NN) method (*59*). In particular, 17 PIPs up to second order have included as the input layer of the NN in order to take advantage of the permutation symmetry of this ABC_2 system. The details of the NN training can be found in ref. (*59*). The fitting is carried out in two different regions:

(a) The reactant asymptotic region V_1: There are 5113 points with the distance between C and O from 4 Å to 50 Å. The NN consists of 2 layers, with 20 and 60 interconnected neurons. The total number of parameters is thus 1681. The RMSE of the fitting is less than 0.05 kcal/mol.

(b) The main region V_2: There are 23749 points with the distance between C and O less than 6 Å. The NN consists of 2 layers, with 30 and 60 interconnected neurons. The total number of parameters is thus 2461. The RMSE of the fitting is less than 0.5 kcal/mol.

The final SR PES V_{SR} is obtained by connecting these two fits with another switching function S_{fit}:

$$V_{fit} = S_{fit}V_1 + (1 - S_{fit})V_2, \quad \text{(S19)}$$

$$S_{fit} = \frac{1-\tanh[3(\xi-5.0)]}{2}, \quad \text{(S20)}$$

As shown in Table S1, the PIP-NN PES faithfully reproduces energies and geometries of the stationary points. The stationary points along the reaction path are also optimized at the CASSCF/6-31G* level, and corrected for dynamical correlations at the multi-reference configuration interaction (MRCI) level with the AVTZ basis set.

Table S2 Energies (kcal/mol) and harmonic frequencies (cm^{-1}) of the stationary points for the $C^+ + H_2O \rightarrow HCO^+/HOC^+ + H$ reaction.

Species	Method	*E* (kcal/mol)	Frequency (cm^{-1})					
			1	2	3	4	5	6
IM1	CASSCF*	-87.2	3491.2	3393.1	1697.0	970.9	863.6	531.8
	UCCSD(T)	-87.7	3568.3	3465.7	1630.1	936.6	899.9	460.0
	PES	-87.5	3570.5	3419.2	1649.3	904.3	876.6	418.7
IM2	CASSCF	-84.9	2508.0	1963.6	825.5	809.1	728.4	76.
	UCCSD(T)	-85.2	2553.8	1934.7	696.0	661.9	661.4	65.8
	PES	-85.4	2630.5	1908.7	759.2	580.8	580.8	111.6
IM3	CASSCF	-140.7	3486.8	3083.2	1660.9	1263.8	1021.8	935.4
	UCCSD(T)	-141.6	3499.0	3064.2	1691.5	1253.5	999.0	951.6
	PES	-141.9	3576.4	3052.4	1671.7	1269.7	1148.0	993.2
IM4	CASSCF	-136.9	3372.5	2872.2	1781.1	1374.9	1146.3	972.5
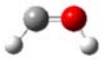	UCCSD(T)	-137.9	3430.3	3044.1	1716.4	1169.4	985.9	924.4
	PES	-137.9	3481.2	3086.4	1653.3	1303.8	1058.2	935.1
IM5	CASSCF	-145.9	2940.8	2818.6	1654.9	1299.4	1076.8	917.5
	UCCSD(T)	-146.3	2905.4	2796.2	1666.7	1260.5	1061.1	846.6
	PES	-146.7	2895.1	2880.2	1686.1	1241.5	1032.0	798.0
IM6	CASSCF	-119.5	3207.4	2181.8	820.9	807.2	215.5	101.7
	UCCSD(T)	-120.7	3015.1	2171.2	900.7	898.9	363.1	152.3
	PES	-121.0	3145.8	2105.1	936.4	936.4	553.0	176.7
TS12	CASSCF	-56.8	3394.9	1496.3	1247.6	819.9	570.0	2477.4i
	UCCSD(T)	-55.6	3439.8	1549.8	1127.4	772.2	463.2	2380.6i
	PES	-56.5	3622.1	1611.3	1229.6	791.3	507.3	2214.7i
TS13	CASSCF	-53.9	3279.5	2303.3	1251.4	997.3	297.5	2133.8i
	UCCSD(T)	-53.7	3328.0	2202.1	1285.9	967.1	155.1i	2057.9i
	PES	-53.9	3231.6	2278.9	1325.9	1045.6	324.3	2121.9i

								
TS34	CASSCF	-121.8	3525.1	3118.5	1656.1	1244.7	860.4	1234.2i
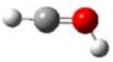	UCCSD(T)	-123.2	3351.8	3243.5	1692.8	1164.5	837.9	1242.1i
	PES	-122.5	3359.9	3057.6	1692.6	1174.8	376.2i	1136.1i
TS35	CASSCF	-97.6	2089.7	1801.5	1180.8	1080.0	989.0	1238.2i
	UCCSD(T)	-101.2	2999.5	2273.6	1712.5	1051.1	678.9	2133.9i
	PES	-102.1	2814.1	2205.3	1785.6	1110.5	874.6	2130.6i
TS4	CASSCF	-97.5	2530.0	1818.5	1084.5	959.0	653.4	1689.3i
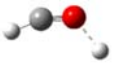	UCCSD(T)	-101.9	3161.8	1954.2	868.7	829.5	652.3	1964.0i
	PES	-102.2	3339.4	1980.8	999.9	859.6	788.3	2328.8i
TS56	CASSCF	-118.9	3977.2	2055.8	1144.7	158.9	987.1i	2584.5i
	UCCSD(T)	-118.0	3196.4	2131.1	939.4	839.3	517.8	673.6i
	PES	-117.3	3248.8	2029.0	865.4	765.5	550.0	909.1i

The geometry optimizations and frequencies analysis by CASSCF/6-31G, and the energies are corrected at the MRCI/AVTZ level.

Because of the large density of states in this system, it is still impractical to investigate the dynamics with a quantum mechanical method. For such an exoergic and barrierless reaction, on the other hand, the QCT approach is reasonable because quantum effects such as tunneling are not expected to be important. The QCT calculations are performed using VENUS (*46*). The trajectories are initiated with a 41.0 Å separation between reactants, and terminated when products reach a separation of 10.0 Å. The largest impact parameter chosen is b_{max}=39 Å to ensure the inclusion of long-range interactions. The propagation time step is 0.05 fs. The total energy conservation is found to be better than 0.04 kcal/mol for all the trajectories. A few trajectories are discarded if the propagation time reached 300 ps. The violation of the product zero-point energy is expected to be minimal due to the large exothermicity of the reaction.

The thermal rate constant can be computed by the following expression:

$$k(T) = \left(\frac{8k_B T}{\pi\mu}\right)^{1/2} \pi b_{max}^2 \frac{N_r}{N_{total}}, \quad \text{(S21)}$$

where μ is the reduced mass between the two reactants, k_B the Boltzmann constant, and T temperature in Kelvin. N_r and N_{total} are the number of reactive trajectories and total number of trajectories, respectively. At the experimental temperatures of 20 K, the initial rotational energies of the water reactant and relative translational energies between C^+ and H_2O are sampled according to the Boltzmann distribution. A total of 48465 trajectories are run at this temperature. The branching ratio is computed from the rate coefficients of the two product channels.

Despite the higher energy of the HOC^+ isomer, the QCT results indicate that it accounts for 97% of the products. The dominance of the HOC^+ product is consistent with the prediction by an earlier room temperature kinetic study (*22*) and direct dynamics studies on the same process using a lower-level *ab initio* theory (*29, 60*). As discussed in the main text, the reaction typically forms a short-lived intermediate (IM1) with the configuration C-OH_2. The transfer of the energy from the C-O mode to O-H mode leads the dissociation to major product H + HOC+ channel. On the other hand, some trajectories fail to break the O-H bond but the energy imparted into the H atom leads to large amplitude motion and the formation of HCOH species, which eventually dissociates into the minor HCO^+ + H channel by cleaving the O-H bond. This is illustrated in Figure S7 where the OH, OH', CO, CH and CH' distances are plotted for two exemplary trajectories leading to these two channels.

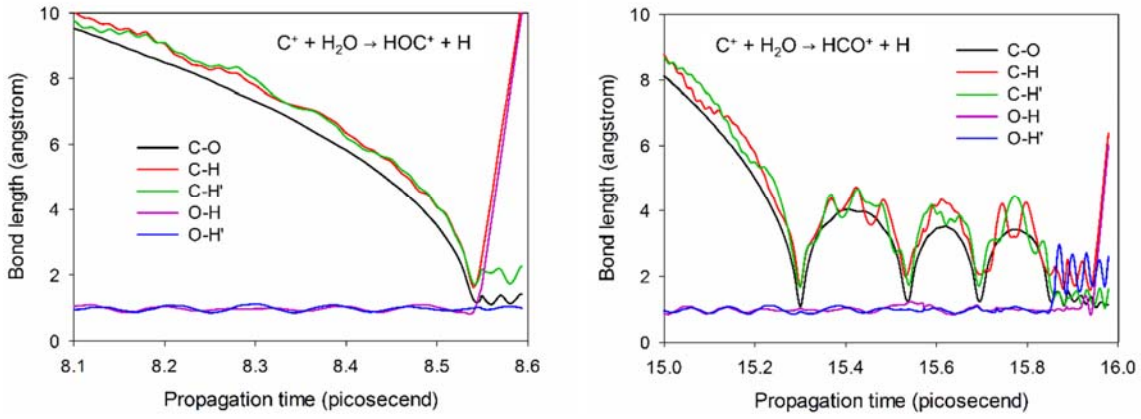

Figure S7. Internuclear distances in two exemplary trajectories leading to HOC^+ + H and HCO^+ + H channels.

6. Isomerization in radiative decay of hot HOC^+/HCO^+ products

Our QCT results on the ground state PES indicate significant internal excitations of both HCO^+ and HOC^+ products. Specifically, 87.8% of HOC^+ and 29.6% of HCO^+ have internal energies above the isomerization barrier. Since these ions are stored in the trap for more than 1 s before the introduction of N_2, any high-lying vibrational states with energy above the barrier would have relaxed via spontaneous emission to lower-lying, below-the-barrier vibrational states (*43, 61*). This relaxation is likely accompanied with isomerization and alters the product branching ratio from the value found in the QCT calculation. This is facilitated by gateway states immediately above the isomerization barrier, which are vibrational eigenstates that possess amplitudes in both the HOC^+ and HCO^+ wells. The formation of such states is facilitated by the accidental degeneracy of zeroth order states associated with the two isomers and anharmonic couplings between them, as illustrated in recent work on the vinylidene-acetylene system (*62*). The radiative decay of such a gateway state will thus lead to population

transfer from one well to another. More importantly, such isomerization is irreversible if the gateway state is just above the isomerization barrier, as the vibrational relaxation can only take place to local vibrational states in the two wells. Unfortunately, a spectroscopically accurate determination of these gateway states and the rest of the highly excited vibrational energy levels is still beyond our capability, despite the availability of the HCO^+/HOC^+ PES (*63*).

The amount of isomerization can be estimated in terms of the density of states (DOS) of the two isomers. The vibrational DOS at the barrier has been calculated for both isomers, based on the harmonic frequencies listed in Table S3. These frequencies are in reasonably good agreement with earlier theory (*63*). Despite the higher energy of HOC^+, it has a higher vibrational DOS (40 /cm^{-1}) at the isomerization barrier than that of HCO^+ (20 /cm^{-1}) due to its extremely low bending frequency. It can thus be estimated based on the DOSs that 33% of the HOC^+ above the barrier would isomerize during its radiative decay, leading to a final HOC^+:HCO^+ ratio of 2.3, in good agreement with the experimental result. As 97% of the initial product population is in the HOC^+ well, on the other hand, it is conceivable that the isomerization is unidirectional, namely the isomerization of above-the-barrier HCO^+, which has an initial population of merely 3%, can be neglected.

Table S3. Calculated energies, geometries, and harmonic frequencies of the HCO^+ and HOC^+

Species	Energy (kcal/mol)	r_{CO} (Å)	r_{CH} (Å)	r_{OH} (Å)	C-O stretching (cm^{-1})	C-H/O-H stretching (cm^{-1})	Bending (cm^{-1})
HCO^+	0	1.108	1.094	2.202	3219	2208	846
HOC^+	44.7	1.159	2.151	0.992	3460	1937	84

REFERENCES AND NOTES

1. Y. Aikawa, V. Wakelam, R. T. Garrod, E. Herbst, Molecular evolution and star formation: From prestellar cores to protostellar cores. *Astrophys J.* **674**, 984–996 (2008).
2. D. J. Hollenbach, A. G. G. M. Tielens, Photodissociation regions in the interstellar medium of galaxies. *Rev. Mod. Phys.* **71**, 173–230 (1999).
3. A. Usero, S. García-Burillo, A. Fuente, J. Martín-Pintado, N. J. Rodríguez-Fernández, Molecular gas chemistry in AGN. *Astron. Astrophys.* **419**, 897–912 (2004).
4. R. Meijerink, M. Spaans, F. P. Israel, Diagnostics of irradiated dense gas in galaxy nuclei. *Astron. Astrophys.* **461**, 793–811 (2007).
5. S. García-Burillo, F. Combes, A. Usero, S. Aalto, M. Krips, S. Viti, A. Alonso-Herrero, L. K. Hunt, E. Schinnerer, A. J. Baker, F. Boone, V. Casasola, L. Colina, F. Costagliola, A. Eckart, A. Fuente, C. Henkel, A. Labiano, S. Matín, I. Márquez, S. Muller, P. Planesas, C. Ramos Almeida, M. Spaans, L. J. Tacconi, P. P. van der Werf, Molecular line emission in NGC 1068 imaged with ALMA. I. An AGN-driven outflow in the dense molecular gas. *Astron. Astrophys.* **567**, A125 (2014).
6. A. Labiano, S. García-Burillo, F. Combes, A. Usero, R. Soria-Ruiz, J. Piqueras López, A. Fuente, L. Hunt, R. Neri, Fueling the central engine of radio galaxies. *Astron. Astrophys.* **564**, A128 (2014).
7. L. R. Liu, J. D. Hood, Y. Yu, J. T. Zhang, N. R. Hutzler, T. Rosenband, K.-K. Ni, Building one molecule from a reservoir of two atoms. *Science* **360**, 900–903 (2018).
8. Y.-P. Chang, K. Długołęcki, J. Küpper, D. Rösch, D. Wild, S. Willitsch, Specific chemical reactivities of spatially separated 3-Aminophenol conformers with cold Ca^+ ions. *Science* **342**, 98–101 (2013).
9. P. Puri, M. Mills, C. Schneider, I. Simbotin, J. A. Montgomery Jr, R. Côté, A. G. Suits, E. R. Hudson, Synthesis of mixed hypermetallic oxide $BaOCa^+$ from laser-cooled reagents in an atom-ion hybrid trap. *Science* **357**, 1370–1375 (2017).
10. S. Willitsch, M. T. Bell, A. D. Gingell, S. R. Procter, T. P. Softley, Cold reactive collisions between laser-cooled ions and velocity-selected neutral molecules. *Phys. Rev. Lett.* **100**, 043203 (2008).
11. J. Deiglmayr, A. Göritz, T. Best, M. Weidemüller, R. Wester, Reactive collisions of trapped anions with ultracold atoms. *Phys. Rev. A* **86**, 043438 (2012).
12. F. H. J. Hall, S. Willitsch, Millikelvin reactive collisions between sympathetically cooled molecular ions and laser-cooled atoms in an ion-atom hybrid trap. *Phys. Rev. Lett.* **109**, 233202 (2012).
13. C. Savage, L. M. Ziurys, Ion chemistry in photon-dominated regions: Examining the $[HCO^+]/[HOC^+]/[CO^+]$ chemical network. *Astrophys J* **616**, 966–975 (2004).
14. L. M. Ziurys, A. J. Apponi, Confirmation of interstellar HOC^+: Reevaluating the $[HCO]^+/[HOC]^+$ abundance ratio. *Astrophys. J.* **455**, L73–L76 (1995).

15. J. Armijos-Abendaño, J. Martín-Pintado, E. López, M. Llerena, N. Harada, M. A. Requena-Torres, S. Martín, V. M. Rivilla, D. Riquelme, F. Aldas, On the effects of UV photons/X-Rays on the chemistry of the Sgr B2 cloud. *Astrophys. J.* **895**, 57 (2020).
16. A. Fuente, S. García-Burillo, A. Usero, M. Gerin, R. Neri, A. L. Faure, J. Bourlot, M. González-García, J. R. Rizzo, T. Alonso-Albi, J. Tennyson, On the chemistry and distribution of HOC^+ in M 82: More evidence for extnsive PDRs. *Astron. Astrophys.* **492**, 675–684 (2008).
17. A. Fuente, S. García-Burillo, M. Gerin, D. Teyssier, A. Usero, J. R. Rizzo, P. de Vicente, Photon-dominated chemistry in the nucleus of M82: Widespread HOC^+ emission in the inner 650 parsec disk. *Astrophys. J.* **619**, L155–L158 (2005).
18. S. Martín, J. Martín-Pintado, S. Viti, Photodissociation chemistry footprints in the starburst galaxy NGC 253. *Astrophys. J.* **706**, 1323–1330 (2009).
19. R. Aladro, S. König, S. Aalto, E. González-Alfonso, N. Falstad, S. Martín, S. Muller, S. García-Burillo, C. Henkel, P. van der Werf, E. Mills, J. Fischer, F. Costagliola, M. Krips, Molecular gas in the northern nucleus of Mrk 273: Physical and chemical properties of the disc and its outflow. *Astron. Astrophys.* **617**, A20 (2018).
20. J. Armijos-Abendaño, J. Martín-Pintado, M. A. Requena-Torres, S. Martín, A. Rodríguez-Franco, 3-mm spectral line survey of two lines of sight towards two typical cloud complexes in the Galactic Centre. *Mon. Not. R Astron. Soc.* **446**, 3842–3862 (2014).
21. R. C. Woods, C. S. Gudeman, R. L. Dickman, P. F. Goldsmith, G. R. Huguenin, W. M. Irvine, A. Hjalmarson, L.-A. Nyman, H. Olofsson, The $[HCO^+]/[HOC^+]$ abundance ratio in molecular clouds. **270**, 583–588 (1983).
22. C. G. Freeman, M. J. McEwan, A selected-ion flow tube study of the $C^+ + H_2O$ reaction. *Int. J. Mass Spectrom. Ion Process* **75**, 127–131 (1987).
23. J. R. Flores, A. B. González, The role of the excited electronic states in the $C^+ + H_2O$ reaction. *J. Chem. Phys.* **128**, 144310 (2008).
24. Å. Larson, A. E. Orel, Electronic resonant states of HCO and HOC. *Phys. Rev. A* **80**, 062504 (2009).
25. D. M. Sonnenfroh, R. A. Curtis, J. M. Farrar, Collision complex formation in the reaction of C^+ with H_2O. *J. Chem. Phys.* **83**, 3958–3964 (1985).
26. J. B. Marquette, B. R. Rowe, G. Dupeyrat, G. Poissant, C. Rebrion, Ion—Polar-molecule reactions: A CRESU study of He^+, C^+, $N^+ + H_2O$, NH_3 at 27, 68 and 163 K. *Chem. Phys. Lett.* **122**, 431–435 (1985).
27. J. O. Martinez Jr, N. B. Betts, S. M. Villano, N. Eyet, T. P. Snow, V. M. Bierbaum, Gas phase study of C^+ reactions of interstellar relevance. *Astrophys. J.* **686**, 1486–1492 (2008).

28. D. J. Defrees, A. D. McLean, E. Herbst, Calculations concerning the HCO^+/HOC^+ abundance ratio in dense interstellar clouds. *Astrophys. J.* **279**, 322–334 (1984).
29. Y. Ishikawa, R. C. Binning Jr, T. Ikegami, Direct ab initio molecular dynamics study of $C^+ + H_2O$. *Chem. Phys. Lett.* **343**, 413–419 (2001).
30. M. A. Smith, S. Schlemmer, J. von Richthofen, D. Gerlich, $HOC^+ + H_2$ isomerization rate at 25 K: Implications for the observed $[HCO^+]/[HOC^+]$ ratios in the interstellar medium. *Astrophys. J.* **578**, L87–L90 (2002).
31. B. R. Rowe, J. B. Marquette, CRESU studies of ion/molecule reactions. *Int. J. Mass Spectrom. Ion Process.* **80**, 239–254 (1987).
32. D. Gerlich, M. Smith, Laboratory astrochemistry: Studying molecules under inter- and circumstellar conditions. *Phys. Scr.* **73**, C25–C31 (2005).
33. W. Paul, Electromagnetic traps for charged and neutral particles. *Rev. Mod. Phys.* **62**, 531–540 (1990).
34. T. Yang, A. Li, G. K. Chen, C. Xie, A. G. Suits, W. C. Campbell, H. Guo, E. R. Hudson, Optical control of reactions between water and laser-cooled Be^+ ions. *J. Phys. Chem. Lett.* **9**, 3555–3560 (2018).
35. G. K. Chen, C. Xie, T. Yang, A. Li, A. G. Suits, E. R. Hudson, W. C. Campbell, H. Guo, Isotope-selective chemistry in the $Be^+(^2S_{1/2}) + HOD \rightarrow BeOD^+/BeOH^+ + H/D$ reaction. *Phys. Chem. Chem. Phys.* **21**, 14005–14011 (2019).
36. D. J. Wineland, W. M. Itano, Laser cooling of atoms. *Phys. Rev. A* **20**, 1521–1540 (1979).
37. E. R. Hudson, Sympathetic cooling of molecular ions with ultracold atoms. *EPJ Tech. Instrum.* **3**, 8 (2016).
38. E. R. Hudson, Method for producing ultracold molecular ions. *Phys. Rev. A* **79**, 032716 (2009).
39. Z. Fang, V. H. S. Kwong, J. Wang, W. H. Parkinson, Measurements of radiative-decay rates of the $2s^22p(^2P^0)$-$2s2p^2(^4P)$ intersystem transition of C^+. *Phys. Rev. A* **48**, 1114–1122 (1993).
40. D. Patterson, J. Rasmussen, J. M. Doyle, Intense atomic and molecular beams via neon buffer-gas cooling. *New J. Phys.* **11**, 055018 (2009).
41. S. J. Schowalter, K. Chen, W. G. Rellergert, S. T. Sullivan, E. R. Hudson, An integrated ion trap and time-of-flight mass spectrometer for chemical and photo-reaction dynamics studies. *Rev. Sci. Instrum.* **83**, 043103 (2012).
42. C. Schneider, S. J. Schowalter, K. Chen, S. T. Sullivan, E. R. Hudson, Laser-Cooling-Assisted mass spectrometry. *Phys. Rev. Applied* **2**, 034013 (2014).

43. G. Mauclaire, J. Lemaire, M. Heninger, S. Fenistein, D. C. Parent, R. Marx, Radiative lifetimes for an ion of astrophysical interest: HCO^+. *Int. J. Mass Spectrom. Ion Process.* **149-150**, 487–497 (1995).
44. N. G. Adams, D. Smith, D. Grief, Reactions of H_nCO^+ ions with molecules at 300 K. *Int. J. Mass Spectrom. Ion Phys.* **26**, 405–415 (1978).
45. A. J. Chalk, L. Radom, Proton-Transport catalysis: A systematic study of the rearrangement of the isoformyl cation to the formyl cation. *J. Am. Chem. Soc.* **119**, 7573–7578 (1997).
46. X. Hu, W. L. Hase, T. Pirraglia, Vectorization of the general Monte Carlo classical trajectory program VENUS. *J. Comput. Chem.* **12**, 1014–1024 (1991).
47. Q. Yao, C. Xie, H. Guo, Competition between proton transfer and proton isomerization in the N_2 + HOC^+ reaction on an Ab Initio-based global potential energy surface. *J. Phys. Chem. A* **123**, 5347–5355 (2019).
48. D. McElroy, C. Walsh, A. J. Markwick, M. A. Cordiner, K. Smith, T. J. Millar, The UMIST database for astrochemistry 2012. *Astron. Astrophys.* **550**, A36 (2013).
49. M. Röllig, N. P. Abel, T. Bell, F. Bensch, J. Black, G. J. Ferland, B. Jonkheid, I. Kamp, M. J. Kaufman, J. Le Bourlot, F. Le Petit, R. Meijerink, O. Morata, V. Ossenkopf, E. Roueff, G. Shaw, M. Spaans, A. Sternberg, J. Stutzki, W.-F. Thi, E. F. van Dishoeck, P. A. M. van Hoof, S. Viti, M. G. Wolfire, A photon dominated region code comparison study. *Astron. Astrophys.* **467**, 187–206 (2007).
50. N. R. Hutzler, H.-I. Lu, J. M. Doyle, The buffer gas beam: An intense, cold, and slow source for atoms and molecules. *Chem. Rev.* **112**, 4803–4827 (2012).
51. P.-Y. Zhao, Z.-X.. Xiong, L. Jie, L.-X. He, B.-L. Lu, Magneto-Optical Trapping of Ytterbium Atoms with a 398.9 nm Laser. *Chin. Phys. Lett.* **25**, 3631–3634 (2008).
52. C. G. Freeman, J. S. Knight, J. G. Love, M. J. McEwan, The reactivity of HOC^+ and the proton affinity of CO at O. *Int. J. Mass Spectrom. Ion Process.* **80**, 255–271 (1987).
53. V. G. Anicich, Evaluated bimolecular ion-molecule gas phase kinetics of positive ions for use in modeling planetary atmospheres, cometary comae, and interstellar clouds. *J. Phys. Chem. Ref. Data Monogr.* **22**, 1469–1569 (1993).
54. NIST, Computational Chemistry Comparison and Benchmark Database, NIST Standard Reference Database Number 101, R. D. Johnson III, Ed. Release 21, August 2020; http://cccbdb.nist.gov/. DOI:10.18434/T47C7Z.
55. G. Knizia, T. B. Adler, H.-J. Werner, Simplified CCSD(T)-F12 methods: Theory and benchmarks. *J. Chem. Phys.* **130**, 054104 (2009).

56. K. A. Peterson, T. B. Adler, H.-J. Werner, Systematically convergent basis sets for explicitly correlated wavefunctions: The atoms H, He, B–Ne, and Al–Ar. *J. Chem. Phys.* **128**, 084102 (2008).
57. A. J. Stone, *The Theory of Intermolecular Forces* (Oxford Univ. Press, ed. 2, 2013).
58. A. D. Buckingham, Permanent and induced molecular moments and long-range intermolecular forces. *Adv. Chem. Phys.* **12**, 107–142 (1967).
59. B. Jiang, J. Li, H. Guo, Potential energy surfaces from high fidelity fitting of ab initio points: The permutation invariant polynomial-neural network approach. *Int. Rev. Phys. Chem.* **35**, 479–506 (2016).
60. J.-i. Yamamoto, Ab initio molecular dynamics simulation on $H_2O + C^+$ reaction. *J. Mol. Struct.* **957**, 55–60 (2010).
61. R. Wester, U. Hechtfischer, L. Knoll, M. Lange, J. Levin, M. Scheffel, D. Schwalm, A. Wolf, A. Baer, Z. Vager, D. Zajfman, M. Mladenović, S. Schmatz, Relaxation dynamics of deuterated formyl and isoformyl cations. *J. Chem. Phys.* **116**, 7000–7011 (2002).
62. J. A. DeVine, M. L. Weichman, B. Laws, J. Chang, M. C. Babin, G. Balerdi, C. Xie, C. L. Malbon, W. C. Lineberger, D. R. Yarkony, R. W. Field, S. T. Gibson, J. Ma, H. Guo, D. M. Neumark, Encoding of vinylidene isomerization in its anion photoelectron spectrum. *Science* **358**, 336–339 (2017).
63. M. Mladenović, S. Schmatz, Theoretical study of the rovibrational energy spectrum and the numbers and densities of bound vibrational states for the system HCO^+/HOC^+. *J. Chem. Phys.* **109**, 4456–4470 (1998).